Angular momentum conservation in spin-lattice dynamics simulations

Joseph R. Cooke, III and Jennifer R. Lukes

Angular Momentum Conservation in Spin-Lattice Dynamics Simulations

Joseph R. Cooke III[1, 2] and Jennifer R. Lukes[1]

[1]*Department of Mechanical Engineering and Applied Mechanics,*
University of Pennsylvania, Philadelphia, Pennsylvania 19104, United States
[2]*Research Computing, ITS Division, Northeastern University, Boston, Massachusetts 02115, United States*
(Dated: December 15, 2022)

Kuzkin's angular momentum balance method is implemented in the LAMMPS SPIN package for atomistic spin-lattice dynamics, along with shifted-force exchange and Néel Hamiltonians parameterized to minimize energy drifts in the simulations. Angular momentum contributions arising from two mechanisms are quantified using this method: particle transport across the boundaries of a periodic simulation domain and external torques applied to the domain by periodic image atoms. When these mechanisms are accounted for, lattice angular momentum is exactly conserved in lattice systems and in spin-lattice systems with isotropic exchange interactions. The calculations show that spin-lattice angular momentum exchange only occurs when the Néel anisotropy energy is added to the exchange energy, and that with this addition, total angular momentum is approximately conserved in the magnetization direction but not in other directions. Inclusion of the Néel anisotropy increases the energy drifts observed in simulations of iron nanoparticles. These drifts are linearly proportional to the magnitude of the anisotropy energy and the simulation time step.

I. INTRODUCTION

Spin-lattice dynamics (SLD) [1–8] is a classical atomistic simulation method for modeling magnetic materials that combines aspects of molecular dynamics (MD) [9, 10] and spin dynamics [11, 12]. In SLD, atomic displacements, velocities, and magnetic moment orientations are advanced in time by integrating the equations of motion. The ability of SLD to track spin and lattice degrees of freedom have made it an attractive method to investigate thermal-magnetic energy conversion processes in a variety of applications, including nanoparticle hyperthermia therapy [7–14], heat assisted magnetic recording for data storage [15–19], and spin caloritronic devices for energy harvesting [20–22].

Angular momentum is an important quantity in SLD simulations. The total angular momentum in SLD, $\mathcal{J}$, is the sum of the system's lattice and spin angular momenta:

$$\mathcal{J}(t) = \mathbf{L}(t) + \mathbf{S}(t). \tag{1}$$

The lattice angular momentum of the system is given by

$$\mathbf{L}(t) = \sum_i^N \mathbf{L}_i \tag{2}$$

where N is the number of atoms in the simulation domain and $\mathbf{L}_i$ is the angular momentum of atom i about the center of mass

$$\mathbf{L}_i = (\mathbf{r}_i - \mathbf{r}_c) \times m_i \mathbf{v}_i. \tag{3}$$

Here $\mathbf{r}_c$ is the position of the center of mass of the domain, and $\mathbf{r}_i$, $\mathbf{v}_i$, and m_i are the the position, velocity, and mass of atom i. The spin angular momentum of the system is written as

$$\mathbf{S}(t) = \sum_i^N \mathbf{S}_i. \tag{4}$$

where $\mathbf{S}_i$ is the spin angular momentum associated with atom i by virtue of its magnetic moment $\boldsymbol{\mu}_i$. This is expressed as

$$\mathbf{S}_i = -\hbar \mathbf{s}_i \tag{5}$$

where $\mathbf{s}_i = \boldsymbol{\mu}_i / \mu_i$ is a unit vector that points in the direction of atom i's magnetic moment vector, $\boldsymbol{\mu}_i$, and μ_i is the magnitude of the magnetic moment. Here we note that we follow Evans et al. [11] in defining $\mathbf{s}_i$ as a unit vector in the direction of the magnetic moment and not a unit vector in the direction of the spin angular momentum. The two unit vectors are oppositely directed and thus differ by a negative sign. Had we defined $\mathbf{s}_i$ as a unit vector in the direction of the spin angular momentum, as is done in Refs [2] and [3], Eq. (5) would have no negative sign.

The transfer of angular momentum between $\mathbf{L}$ and $\mathbf{S}$ is necessary to ensure thermalization of spin and lattice subsystems to the same temperature [3, 6] and to capture magnetostrictive behavior [5]. While the importance of angular momentum transfer has been discussed by several groups [3, 5–7, 13], only two [7, 13] directly calculate angular momentum and analyze its exchange between spin and lattice systems. Both these studies were performed on isolated nanoparticles. Aßmann and Nowak [7] applied a 50 T magnetic field to a cubical cobalt particle with free boundaries, and observed particle rotation consistent with the Einstein-de Haas effect. They also calculated the time-dependent angular momenta of spin and lattice systems and showed that their sum, total angular momentum $\mathcal{J}$, was conserved in the direction of the applied magnetic field. Dednam et al. [13] calculated $\mathcal{J}$, $\mathbf{L}$, and $\mathbf{S}$ for a prolate spheroid-shaped iron nanoparticle. They found that the magnitude of angular momentum was conserved in the absence of a magnetic field.

Calculations of angular momentum exchange have not yet been reported for bulk magnetic materials despite

the prevalence of these materials in the SLD literature [1, 3, 6, 8]. It is well known that MD simulations employing periodic boundary conditions, which are required to model bulk materials, do not conserve lattice angular momentum [9, 14] due to the interaction of the main computational cell with its periodic images [14]. Kuzkin [14] addressed the lack of lattice angular momentum conservation in bulk MD simulations by treating the main simulation domain as an open system. Angular momentum is transported into and out of the domain by atoms that cross its boundaries, and angular momentum is generated in the domain by atoms in the periodic images that apply forces that torque it about its center of mass. By accounting for boundary transport and periodic image source terms, Kuzkin showed that lattice angular momentum is conserved in an open MD system context.

In contrast, SLD algorithms currently used in the literature do not include these terms, although they do include a different source of lattice angular momentum that arises from the magnetic anisotropy: spin-lattice coupling. Without the boundary and periodic image terms, the angular momentum bookkeeping in bulk systems is not properly handled. Owing to these terms, the increase in lattice angular momentum is not in general equal to the decrease in spin angular momentum, unlike the nanoparticles studied in Refs. [7, 13]. Handling these terms correctly will enable a clear understanding of the precise amount of angular momentum transfer between spin and lattice systems, which is important for modeling thermalization rates [3] and ultrafast magnetization dynamics [6].

Here we implement Kuzkin's method in SLD for the first time, to enable proper accounting of lattice angular momentum in bulk systems. Specifically, we implement it in the SPIN package [1] in LAMMPS [15], and analyze the spin and lattice angular momentum in iron systems governed by embedded atom method (EAM), exchange, and Néel interactions. The equations of motion for SLD are shown in Section II, along with the details of the parameterization and "shifted force" magnetic Hamiltonians used in this work. The theoretical foundation of the angular momentum calculations and the implementation of Kuzkin's method in the Suzuki-Trotter decomposition used in the SPIN package's explicit solver are given in Section III. Angular momenta calculated with our method for lattice and spin-lattice systems are discussed in Sections IV and V, respectively, for both bulk materials and nanoparticles. The energy stability of our SLD method is reported in Section VI and the conclusions are presented in Section VII.

II. THEORY

A. Equations of Motion

The SLD equations of motion solved in the microcanonical ensemble are [1, 2]

$$\frac{d\mathbf{r}_i}{dt} = \mathbf{v}_i \tag{6}$$

$$\frac{d\mathbf{v}_i}{dt} = \frac{\mathbf{f}_i}{m_i} \tag{7}$$

$$\frac{d\mathbf{s}_i}{dt} = \boldsymbol{\omega}_i \times \mathbf{s}_i. \tag{8}$$

The variables $\mathbf{r}_i$, $\mathbf{v}_i$, and m_i are the position, velocity, and mass of atom i. The force acting on atom i, $\mathbf{f}_i$, is calculated from the negative gradient of the total Hamiltonian, $\mathcal{H}$, with respect to $\mathbf{r}_i$:

$$\mathbf{f}_i = -\frac{\partial \mathcal{H}}{\partial \mathbf{r}_i}. \tag{9}$$

Here $\boldsymbol{\omega}_i$ is the spin precession angular frequency vector for atom i. This vector is calculated by taking the negative gradient of the Hamiltonian with respect to $\mathbf{s}_i$:

$$\boldsymbol{\omega}_i = -\frac{1}{\hbar}\frac{\partial \mathcal{H}}{\partial \mathbf{s}_i}. \tag{10}$$

As in Eq. (5), the negative sign in Eq. (10) arises from the definition of $\mathbf{s}_i$ as a unit vector in the direction of the magnetic moment.

The total Hamiltonian for a spin lattice dynamics system is comprised of the energies from the atomic lattice and the spin systems [1, 2]:

$$\mathcal{H} = \mathcal{H}_{lattice} + \mathcal{H}_{spin}. \tag{11}$$

The Hamiltonian for the lattice system is defined as

$$\mathcal{H}_{lattice} = \mathcal{H}_{PE} + \mathcal{H}_{KE} \tag{12}$$

where $\mathcal{H}_{PE}$ is the lattice potential energy and $\mathcal{H}_{KE}$ is the kinetic energy of the atoms. In this work, the lattice potential energy is described by the embedded atom method (EAM) potential of Chamati et al. [16] and the kinetic energy of the system is calculated by summing the kinetic energy over all N atoms:

$$\mathcal{H}_{KE} = \frac{1}{2}\sum_i^N m_i(\mathbf{v}_i \cdot \mathbf{v}_i). \tag{13}$$

In the present work, $\mathcal{H}_{spin}$ includes energetic contributions from exchange and Néel anisotropy

$$\mathcal{H}_{spin} = \mathcal{H}_{exch} + \mathcal{H}_{Neel}. \tag{14}$$

B. Parameterization of Magnetic Hamiltonian

Energy drift is a known issue in SLD simulations [1, 5]. In MD this issue has been mitigated by performing a "shifted force" modification to the potential to ensure that both the energy and force go smoothly to zero at the cutoff radius [9, 17]. We extend this idea to the exchange and Néel Hamiltonians in order to avoid discontinuities in magnetic energies and forces at the cutoff. For the exchange Hamiltonian, the shifted force modification is implemented by replacing the Bethe-Slater distance dependent exchange energy term used previously [1, 5, 18]

$$J(r_{ij}) = 4\alpha_e \left(\frac{r_{ij}}{\delta_e}\right)^2 \left(1 - \gamma_e \left(\frac{r_{ij}}{\delta_e}\right)^2\right) e^{-\left(\frac{r_{ij}}{\delta_e}\right)^2} \quad (15)$$

with the shifted force exchange energy $J_{SF}(r_{ij})$

$$J_{SF}(r_{ij}) = \left[J(r_{ij}) - J(r_c) - \left[\frac{dJ(r_{ij})}{dr_{ij}}\right]_{r_{ij}=r_c} (r_{ij} - r_c) \right] \Theta(r_c - r_{ij}). \quad (16)$$

In Eq. 16, the energy shift is performed by subtracting the energy of the function at the cutoff, and the force shift is performed by subtracting the product of $r_{ij} - r_c$ and the first derivative of energy at the cutoff [4]. Other shifted force potentials have been applied for the exchange energy, either by selecting a functional form whose value and first derivative are automatically zero at the cutoff [2], or by using a smoothing function [5]. The exchange Hamiltonian with the shifted force exchange energy is thus written as

$$\mathcal{H}_{exch} = -\frac{1}{2} \sum_{i,j=1,i\neq j}^{N} J_{SF}(r_{ij})(\mathbf{s}_i \cdot \mathbf{s}_j - 1). \quad (17)$$

The second term in Eq. (17) represents the ground state magnetic energy (fully aligned spins) at the given atomic configuration. It is subtracted from the combined spin-lattice Hamiltonian because it is already accounted for in the lattice potential energy [1–3]. Following Ma et al. [2], we subtract the ground state exchange energy from the exchange Hamiltonian, rather than from the potential energy [1, 3]. The implication of this is that the exchange Hamiltonian captures the effect of atomic spin orientations on energy, while the EAM captures the effect of atomic displacements on energy.

The Néel anisotropy energy [1, 5, 18] is used in this work because it has been shown to accurately represent the magnetocrystalline anisotropy energy in cubic crystals [18], and because it has been used in other recent studies to model anisotropy [5, 6]. Including a pseudo-dipole term, $l_1(r_{ij})$, and two pseudo-quadrupole terms,

$q_1(r_{ij})$ and $q_2(r_{ij})$, it is expressed as

$$\mathcal{H}_{Neel} = -\frac{1}{2} \sum_{i,j=1,i\neq j}^{N} \left(l_1(r_{ij}) \left[(\mathbf{e}_{ij} \cdot \mathbf{s}_i)(\mathbf{e}_{ij} \cdot \mathbf{s}_j) - \frac{\mathbf{s}_i \cdot \mathbf{s}_j}{3} - \frac{2}{3} \right] + q_1(r_{ij}) \left(\left[(\mathbf{e}_{ij} \cdot \mathbf{s}_i)^2 - \frac{\mathbf{s}_i \cdot \mathbf{s}_j}{3} \right] \left[(\mathbf{e}_{ij} \cdot \mathbf{s}_j)^2 - \frac{\mathbf{s}_i \cdot \mathbf{s}_j}{3} \right] - \frac{4}{9} \right) + q_2(r_{ij})[(\mathbf{e}_{ij} \cdot \mathbf{s}_i)(\mathbf{e}_{ij} \cdot \mathbf{s}_j)^3 + (\mathbf{e}_{ij} \cdot \mathbf{s}_j)(\mathbf{e}_{ij} \cdot \mathbf{s}_i)^3] - 2 \right). \quad (18)$$

where $\mathbf{e}_{ij} = \mathbf{r}_{ij}/r_{ij} = (\mathbf{r}_i - \mathbf{r}_j)/r_{ij}$ is the normalized unit vector from atom j to atom i. As with the exchange energy, we subtract the ground state Néel anisotropy energy from the usual Néel Hamiltonian. This gives rise to the -2/3, -4/9, and -2 terms in Eq. 18. The individual energy terms are defined as

$$l_1(r_{ij}) = l_{SF}(r_{ij}) + \frac{12}{35} q_{SF}(r_{ij}) \quad (19)$$

$$q_1(r_{ij}) = \frac{9}{5} q_{SF}(r_{ij}) \quad (20)$$

$$q_2(r_{ij}) = -\frac{2}{5} q_{SF}(r_{ij}) \quad (21)$$

where $l_{SF}(r_{ij})$ and $q_{SF}(r_{ij})$ are the shifted force dipole and quadrupole energies

$$l_{SF}(r_{ij}) = \left[l(r_{ij}) - l(r_c) - \left[\frac{dl(r_{ij})}{dr_{ij}}\right]_{r_{ij}=r_c} (r_{ij} - r_c) \right] \Theta(r_c - r_{ij}) \quad (22)$$

and

$$q_{SF}(r_{ij}) = \left[q(r_{ij}) - q(r_c) - \left[\frac{dq(r_{ij})}{dr_{ij}}\right]_{r_{ij}=r_c} (r_{ij} - r_c) \right] \Theta(r_c - r_{ij}). \quad (23)$$

The Bethe-Slater functions $l(r_{ij})$ and $q(r_{ij})$

$$l(r_{ij}) = 4\alpha_l \left(\frac{r_{ij}}{\delta_l}\right)^2 \left(1 - \gamma_l \left(\frac{r_{ij}}{\delta_l}\right)^2\right) e^{-\left(\frac{r_{ij}}{\delta_l}\right)^2} \quad (24)$$

$$q(r_{ij}) = 4\alpha_q \left(\frac{r_{ij}}{\delta_q}\right)^2 \left(1 - \gamma_q \left(\frac{r_{ij}}{\delta_q}\right)^2\right) e^{-\left(\frac{r_{ij}}{\delta_q}\right)^2} \quad (25)$$

have unique parameterization constants α_l, δ_l and γ_l for $l(r_{ij})$ and α_q, δ_q and γ_q for $q(r_{ij})$.

We obtained the parameters in Eqs. (24) and (25) following a similar procedure to that of Nieves et al. [18], who fit Bethe-Slater dipole and quadrupole energies to experimentally measured magnetostriction data for iron. First, δ_l and δ_q were set to the nearest neighbor distance r_0:

$$\delta_l = \delta_q = r_0. \tag{26}$$

Then, to obtain the values of α_l, γ_l, α_q, and γ_q, $l_{SF}(r_{ij})$, $q_{SF}(r_{ij})$, $dl_{SF}(r_{ij})/dr_{ij}$, and $dq_{SF}(r_{ij})/dr_{ij}$ were evaluated at the nearest neighbor distance and equated to terms containing the experimentally measured magnetoelastic coupling constants b_1 and b_2:

$$l_{SF}(r_0) = -\frac{3V_0 b_1}{8\mathcal{N}} \tag{27}$$

$$\left(\frac{\partial l_{SF}}{\partial r_{ij}}\right)_{r=r_0} = \frac{3V_0}{8\mathcal{N}r_0}(b_1 - 3b_2) \tag{28}$$

$$q_{SF}(r_0) = -\frac{\sqrt{3}}{4}r_0^3 K_1(r_0) \tag{29}$$

$$\left(\frac{\partial q_{SF}}{\partial r_{ij}}\right)_{r=r_0} = -\frac{3\sqrt{3}}{4}r_0^2 K_1(r_0)\left[1 - \frac{B}{K_1}\frac{\partial K_1}{\partial P}\right]_{r=r_0}. \tag{30}$$

In the above equations, which are appropriate for body-centered cubic crystals, the other parameters are defined as follows. V_0 is the equilibrium volume of the unit cell, $\mathcal{N}$ is the number of atoms in the unit cell, K_1 is the lowest order cubic magnetocrystalline anisotropy energy, B is the bulk modulus, and P is the pressure [18].

This process results in two equations containing α_l and γ_l, and two equations containing α_q and γ_q. Solving this system of equations yields

$$\alpha_l = -\frac{e\left(-2r_c^5(l_0 - r_0 l_0') + 4r_0^2 r_c^3(l_0 - r_0 l_0') + r_0^5 e^{[(\frac{r_c}{r_0})^2 - 1]}(r_0 l_0' - 2l_0) - 2r_c^6 l_0' + 3r_0^2 r_c^4 l_0'\right)}{8\left(e^{[(\frac{r_c}{r_0})^2 - 1]}r_0^5 - r_0^4 r_c + r_0^3 r_c^2 - r_0^2 r_c^3 - 2r_0 r_c^4 + r_c^5\left(1 + e^{-[(\frac{r_c}{r_0})^2 - 1]}\right)\right)} \tag{31}$$

$$\gamma_l = \frac{r_0^2\left(2r_0^2 r_c(l_0 - r_0 l_0') - 2r_c^3(l_0 - r_0 l_0') + r_0^4 e^{[(\frac{r_c}{r_0})^2 - 1]}l_0' + r_0^2 r_c^2 l_0' - 2r_c^4 l_0'\right)}{-2r_c^5(l_0 - r_0 l_0') + 4r_0^2 r_c^3(l_0 - r_0 l_0') + r_0^3 e^{[(\frac{r_c}{r_0})^2 - 1]}(r_0^3 l_0' - 2l_0 r_0^2) - 2r_c^6 l_0' + 3r_0^2 r_c^4 l_0'}. \tag{32}$$

$$\alpha_q = -\frac{e\left(-2r_c^5(q_0 - r_0 q_0') + 4r_0^2 r_c^3(q_0 - r_0 q_0') + r_0^5 e^{[(\frac{r_c}{r_0})^2 - 1]}(r_0 q_0' - 2q_0) - 2r_c^6 q_0' + 3r_0^2 r_c^4 q_0'\right)}{8\left(e^{[(\frac{r_c}{r_0})^2 - 1]}r_0^5 - r_0^4 r_c + r_0^3 r_c^2 - r_0^2 r_c^3 - 2r_0 r_c^4 + r_c^5\left(1 + e^{-[(\frac{r_c}{r_0})^2 - 1]}\right)\right)} \tag{33}$$

$$\gamma_q = \frac{r_0^2\left(2r_0^2 r_c(q_0 - r_0 q_0') - 2r_c^3(q_0 - r_0 q_0') + r_0^4 e^{[(\frac{r_c}{r_0})^2 - 1]}q_0' + r_0^2 r_c^2 q_0' - 2r_c^4 q_0'\right)}{-2r_c^5(q_0 - r_0 q_0') + 4r_0^2 r_c^3(q_0 - r_0 q_0') + r_0^3 e^{[(\frac{r_c}{r_0})^2 - 1]}(r_0^3 q_0' - 2q_0 r_0^2) - 2r_c^6 q_0' + 3r_0^2 r_c^4 q_0'}. \tag{34}$$

In the above expressions, l_0, q_0, l_0', and q_0' are shorthand for $l_{SF}(r_0)$, $q_{SF}(r_0)$, $(dl_{SF}/dr_{ij})_{r_{ij}=r_0}$, and $(dq_{SF}/dr_{ij})_{r_{ij}=r_0}$ and e is Euler's number.

Table I shows the parameterizations obtained with this procedure, using the iron parameters in Ref. [18]. Note that in the present work, the shifted force energies l_{SF} (Eq. 22) and q_{SF} (Eq. 23) have been parameterized, rather than the unshifted Bethe-Slater curves used in Ref. [18], to ensure that energy and force smoothly approach zero at the cutoff. The exchange parameters J_{SF} were obtained from the shifted force parameterization in Ref. [4]. Figure 1 displays the energy scale and distance

dependence of the dipole and quadrupole energies computed using the values in Table I.

Magnetic Energy	α [meV]	γ [-]	δ [Å]	r_c [Å]
J_{SF}	56.57	0.1505	1.72	4.5
l_{SF}	115.651	1.58147	2.4690386	2.6
q_{SF}	-7.47376	1.47921	2.4690386	2.6

TABLE I: Shifted force parameterizations for exchange [4], pseudo-dipole, and pseudo-quadrupole energies.
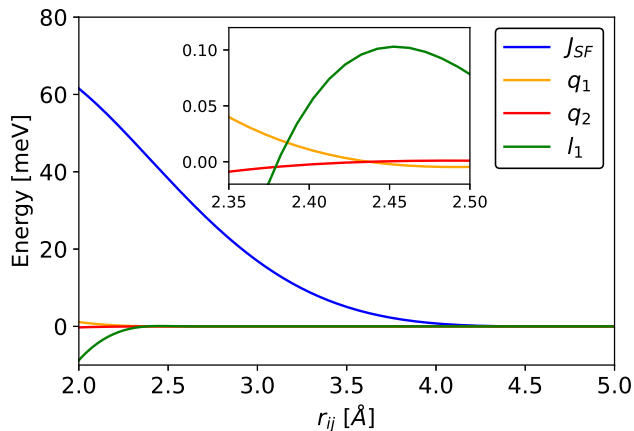
FIG. 1: The exchange, pseudo-dipole, and pseudo-quadrupole energies graphed using the parameterization from Table I.

III. ANGULAR MOMENTUM

A. Theory

The lattice angular momentum balance equation for an open system is

$$\frac{d\mathbf{L}}{dt} = \mathbf{T} + \mathbf{Q} \qquad (35)$$

where $d\mathbf{L}/dt$ is the rate of change of lattice angular momentum, $\mathbf{T}$ is the torque applied to the system by atoms in the periodic images, and $\mathbf{Q}$ is the net transport of lattice angular momentum across the boundaries into the system.

While appropriate for pure MD systems, this expression does not include the lattice angular momentum source term that results from coupling to the spin system. For SLD, the expression is amended to read

$$\frac{d\mathbf{L}}{dt} = \mathbf{T}_{spin} + \mathbf{T} + \mathbf{Q} \qquad (36)$$

where $\mathbf{T}_{spin} = -d\mathbf{S}/dt$ represents the torque exerted on the lattice as a result of angular momentum loss from the spin system. Note that Eq. (36) applies generally to MD and SLD systems, whether they are bulk materials or isolated nanoparticles. For pure MD, the $\mathbf{T}_{spin}$ term is zero since no spins are included, and for isolated particles, the $\mathbf{T}$ and $\mathbf{Q}$ terms are zero because there are no periodic images to add external torques or to act as reservoirs for particles that enter or leave the system through the boundary.

Integration leads to the following expression for the lattice angular momentum at time $t + \Delta t$

$$\mathbf{L}(t + \Delta t) = \mathbf{L}(t) - \Delta \mathbf{S} + \int_t^{t+\Delta t} (\mathbf{T} + \mathbf{Q}) dt, \qquad (37)$$

where $\Delta \mathbf{S} = \mathbf{S}(t + \Delta t) - \mathbf{S}(t)$. A forward difference is used in this expression instead of the central difference used by Kuzkin [14] to enable implementation in the explicit integration scheme in LAMMPS. This allows these quantities to be calculated on the fly in the simulations.

The spin torque term $\mathbf{T}_{spin}$ arises automatically in SLD from Suzuki-Trotter [1–3, 5, 6, 19] or implicit [4, 20] integration schemes. The time-dependent torque from the periodic images is calculated as

$$\mathbf{T}(t) = \sum_i^N (\mathbf{r}_i - \mathbf{r}_c) \times \mathbf{f}_{image,i} \qquad (38)$$

where the image force on atom i is computed by summing the pair forces $\mathbf{f}_{ij}$ exerted on i by the subset of atoms j that are in the periodic images Λ_{im}:

$$\mathbf{f}_{image,i} = \sum_{j \in \Lambda_{im}} \mathbf{f}_{ij}. \qquad (39)$$

The center of mass position $\mathbf{r}_c$ is recalculated at each time step. The torque is integrated using the trapezoidal rule

$$\int_t^{t+\Delta t} \mathbf{T}(t) dt = \frac{\Delta t}{2} (\mathbf{T}(t) + \mathbf{T}(t + \Delta t)) \qquad (40)$$

and the transport term is integrated as follows [14]

$$\int_t^{t+\Delta t} \mathbf{Q}(t) dt = \sum_{i \in \Lambda_+} \mathbf{r}_i \times m_i \mathbf{v}_i - \sum_{i \in \Lambda_-} \mathbf{r}_i \times m_i \mathbf{v}_i. \quad (41)$$

The first term in this expression is summed over all atoms (Λ_+) that re-enter the main simulation domain after exiting the opposite side of the domain. It represents the transport of angular momentum into the domain that arises from the "wrapping" of atomic positions due to the periodic boundary conditions. Similarly, the second term, which is summed over all atoms (Λ_-) that exit the domain, represents the transport of angular momentum out of the domain. Note that the positions in the first and second terms differ by a periodic box length in the wrapping direction(s), with $\mathbf{r}_i$ in the first term being evaluated after the wrapping of the atom and $\mathbf{r}_i$ in the second being evaluated before wrapping. The velocities in both terms are the same, and are evaluated at $t + \Delta t/2$, which is when the atoms cross the boundary. We note that there is no spin angular momentum transport term equivalent to Eq. (41). While atoms do carry spin angular momentum as they cross boundaries, this angular momentum is independent of the atom's position. The spin angular momentum leaving one boundary is the same as that entering on the other side, so the net spin angular momentum flux is zero.

The term $\mathbf{L}(t + \Delta t)$ in Eq. (37) represents the true angular momentum of the computational cell at time $t + \Delta t$. It is convenient to modify this angular momentum

by removing the periodic boundary effects embodied by the integral terms:

$$\mathbf{L}_{corr}(t + \Delta t) = \mathbf{L}(t + \Delta t) - \int_{t}^{t+\Delta t} (\mathbf{T} + \mathbf{Q})dt. \quad (42)$$

This modified angular momentum, which represents the updated lattice angular momentum arising solely from coupling with the spin system in the absence of open system effects, will be compared to spin angular momentum in Section IV.

IV. LATTICE ANGULAR MOMENTUM CONSERVATION IN MOLECULAR DYNAMICS

To demonstrate the validity of our implementation of Kuzkin's method, which is discussed in the Appendix, we first performed a pure MD simulation with the Chamati EAM potential for iron, neglecting spin interactions. Three geometries were investigated and compared in this study: a periodic array of cubes of side length 6a (lattice constant a = 2.8665 Å) and periodicity 12a, a periodic array of cubes of side length 10a and periodicity 12a, and a bulk system with periodicity 12a. The intent of this comparison is to illustrate the contributions of the **T** and **Q** terms in the lattice angular momentum balance equation. Figs. 2(a)-(c) depict these geometries, showing the extent of the main simulation box (black line), the EAM cutoff distance with respect to the outermost layer of atoms (purple line), the atoms inside the main simulation box (blue markers), and atoms in the periodic images (orange markers). It is evident that the 6a cubes in Fig. 2(a) are isolated from one another, as the shortest distance between cube faces exceeds the cutoff distance. In contrast, the 10a cubes in Fig. 3(b) interact with each other because their faces are within the cutoff distance. However, their face-face spacing is too large for atoms to be transported from one cube to the next. Finally, the main simulation box in Fig. 3(c) experiences both interactions with and atomic transport to/from the surrounding bulk in which it is embedded.

Simulations of the three geometries were performed on a single processor using a time step of 0.1 fs. Each geometry was initialized by thermostatting to 100 K for 5 ps with a Langevin thermostat. After 5 ps the thermostat was turned off and the system was run in the NVE ensemble. The angular momentum is calculated for each of the configurations and plotted after the 5 ps thermalization period in Figs. 2 (d) - (f). The angular momentum components start with small nonzero values because the Langevin thermostat does not conserve angular momentum, but after the thermostat is turned off at 5 ps the angular momentum for the purely isolated cube in Fig. 2(d) is conserved. For the other geometries in Figs. 3(e) and 3(f), the angular momentum changes with time. These changes come from the torque exerted on the main simulation box by the image atoms and, for the bulk geometry, atomic transport across the periodic

boundaries arising from oscillation of surface atoms back and forth across the faces of the main simulation box. These results are qualitatively similar to Kuzkin's results for bulk liquids, whose angular momentum also oscillates around an initial value.. Figs. 2(g)-(i) show the torque contributions to angular momentum (Eq. (40)) for each geometry. This contribution is zero for the isolated particle (Fig. 2(g)) because **T** = 0 for that case, and is nonzero for the other two configurations. Figs. 2(j)-(l) show the transport contributions to angular momentum (Eq. (41)) for each geometry. This contribution is zero for the isolated and 10a particles (Figs. 2(j) and 2(k)) because **Q** = 0 for those cases, and is nonzero for the bulk configuration (Fig. 2(l)). Figs. 2(m)-(o) show the modified angular momentum $\mathbf{L}_{corr}$ computed using Eq. (42). For all geometries, it is seen that $\mathbf{L}_{corr}$ is constant, which means that angular momentum is conserved in an open system context.

V. TOTAL ANGULAR MOMENTUM CONSERVATION IN SPIN-LATTICE DYNAMICS

A. EAM and Exchange

Next, we investigate open system angular momentum conservation in isolated cubes and bulk materials when spin interactions are included in addition to the lattice interactions. The geometries modeled in SLD differ in size from those for MD shown in Fig. 2. Larger sizes were used because it was found that the stencil used to decompose the geometry spatially in the SPIN package did not work well below dimensions of 10a when an exchange cutoff of 4.5 Å was used. Accordingly, the isolated cube edge length and periodicity were set to 10a and 20a, respectively. The bulk system periodicity was set to 10a.

We study two SLD cases with different types of spin interactions: one with exchange only and one with exchange and Néel interactions. All SLD simulations unless otherwise stated are run on a single processor with a timestep of 0.1 fs using the Chamati EAM potential, and are initialized with all moments magnetized in the z direction and all atoms placed on the 0 K lattice positions. Langevin thermostats are used to heat both the spin and lattice systems to 100 K for the first 5 ps. For the first SLD case we use the shifted force exchange Hamiltonian in Eq. (17). We monitor the time dependence of three types of angular momentum: modified lattice angular momentum $\mathbf{L}_{corr}$, spin angular momentum **S**, and total angular momentum $\mathbf{L}_{corr} + \mathbf{S}$. These momenta are measured relative to a datum value taken as the value at 5 ps, and their components are plotted for both isolated cube (Figs. 3(a)-(c)) and bulk periodic (Figs. 3(d)-(f)) systems.

For both the isolated cube and the bulk system, spin angular momentum shows much larger fluctuations than lattice angular momentum. ΔL_{corr} appears constant in Fig. 4, with fluctuations on the order 10^{-13} to 10^{-12}
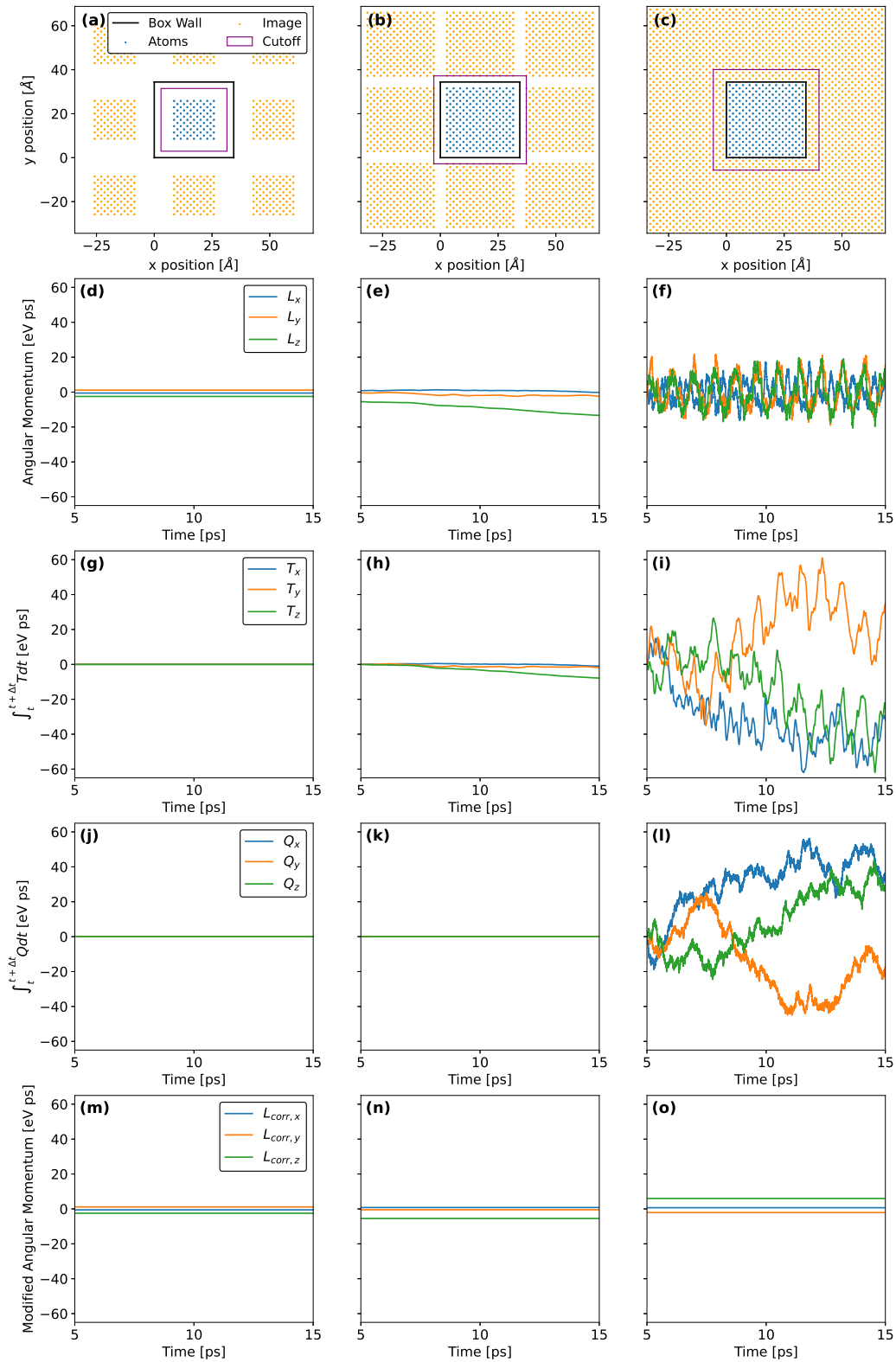
FIG. 2: (a) 6 a cube centered in a periodic 12 a domain, (b) 10 a cube centered in a periodic 12 a domain, and (c) bulk material in a periodic 12 a domain. (d-f): $\mathbf{L}$, the angular momentum about the center of mass for the collection of atoms in the black box for geometries (a-c), respectively. (g-i): integrated torques from the image atoms acting on the main simulation box in geometries (a-c). (j-l): angular momentum flux from atoms wrapping around due to the periodic boundary condition for geometries (a-c). (m-o): $\mathbf{L}_{corr}$, the modified angular momentum for geometries (a-c). All results are based on the EAM Hamiltonian.

eV ps. Spin angular momentum should be conserved under the isotropic exchange interaction, and we attribute the fluctuations in ΔS to errors in the numerical integration algorithm. The fact that these fluctuations are not mirrored by fluctuations in ΔL_{corr} of similar magnitude indicates that the spin and angular momenta are not coupled when only the exchange interactions are considered. This is a consequence of the rotational symmetry of the exchange Hamiltonian [3, 6, 13]. Since the exchange interaction is isotropic, the magnetic forces that it exerts on atoms have no effect on lattice angular momentum because they are central forces pointed along the i-j bond.
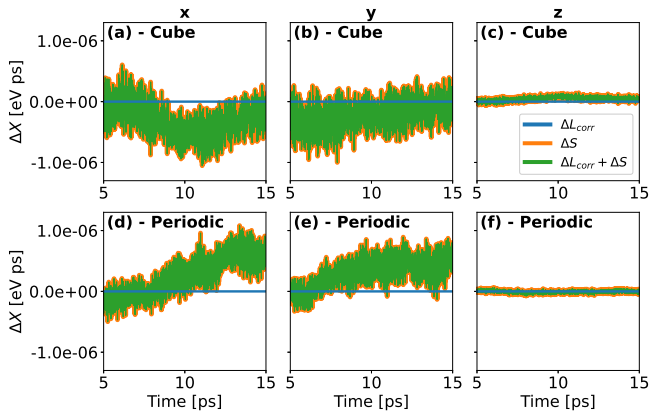

FIG. 3: Different types of relative angular momentum $\Delta X = X(t) - X(5ps)$: modified lattice angular momentum, spin angular momentum, and total open system angular momentum. The x-, y-, and z-components are plotted for isolated cube (a-c) and bulk geometries (d-f) using the EAM and shifted force exchange Hamiltonians.

B. EAM, Exchange, and Néel

The addition of anisotropy to the magnetic Hamiltonian enables coupling of spin and lattice angular momentum [3, 5, 7]. Anisotropy energy depends on the vector between atoms i and j and thus can produce magnetic forces with components normal to $\mathbf{r}_{ij}$, which are able to torque the bonds and alter the lattice angular momentum. Here the Néel anisotropy energy (Eq. (18), with parameters taken from Table I) is added to the total Hamiltonian using the same geometries as in Section V A. The results for the cube geometry are displayed in Figs. 4(a-c). In contrast to the exchange-only result, it is now observed that lattice angular momentum changes with time. In particular, these changes occur in concert with and roughly opposite to those of the spin angular momentum. It is observed that the total angular momentum is not perfectly conserved, with varying amounts of drift in the x, y, and z directions, but that it is better conserved in the z spatial direction.

The isolated particle displays total angular momen-

tum drifts that are larger than those in previous reports [7, 13]. The source of this discrepancy is not understood, but might be related to the different functional forms for anisotropy or to the unspecified time steps used in these works. We note that the drifts are strongly affected by the magnitude of the anisotropy energy. When dipole and quadrupole anisotropy energies α_l and α_q are reduced to 10% of the fitted value in Table I (Figs. 4(d-f)), they are strongly reduced, and when α_l and α_q are reduced to 1% of the fitted value in Table I (Figs. 4(g-i)), they become negligible. The bulk periodic system (Fig. 5) displays similar behavior to that of the isolated particle, albeit with weaker fluctuations that may arise from the lack of a free surface.
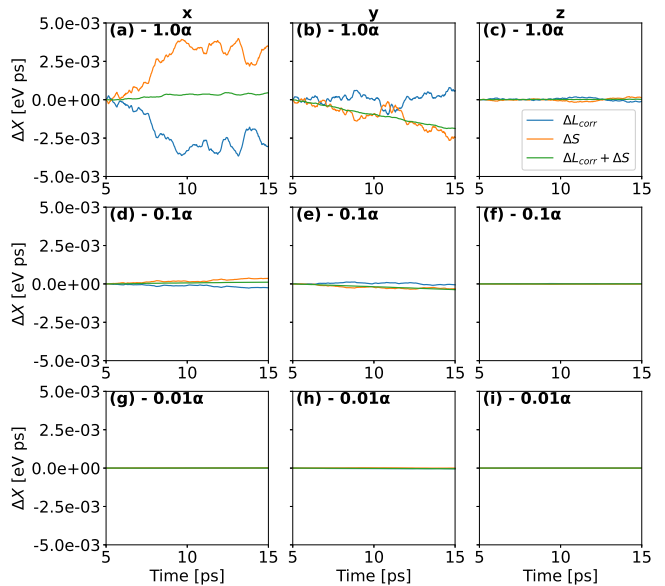

FIG. 4: Relative values of modified lattice angular momentum, spin angular momentum, and total open system angular momentum for an isolated cube using the EAM, shifted force exchange, and shifted force Néel Hamiltonians. The x-, y-, and z components of angular momentum are shown for (a-c) the fitted Néel energy scale given in Table I, (d-f) 10% of the fitted Néel energy, and (g-i) 1% of the fitted Néel energy.
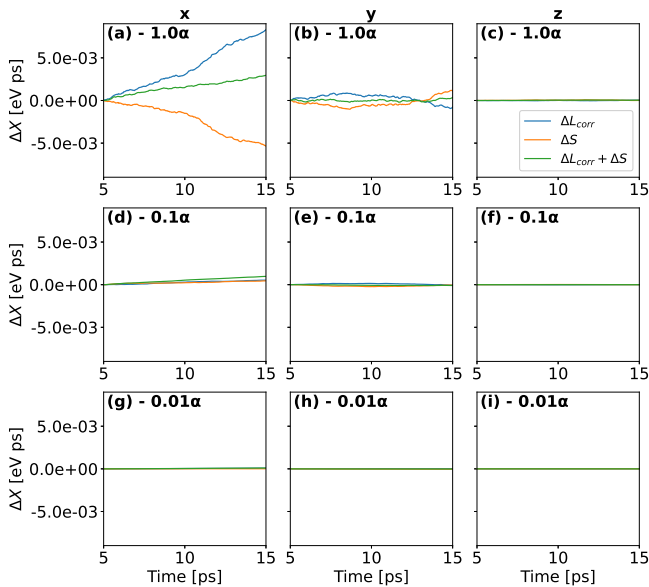
FIG. 5: Relative values of modified lattice angular momentum, spin angular momentum, and total open system angular momentum for a periodic system using the EAM, shifted force exchange, and shifted force Néel Hamiltonians. The x-, y-, and z components of angular momentum are shown for (a-c) the fitted Néel energy scale given in Table I, (d-f) 10% of the fitted Néel energy, and (g-i) 1% of the fitted Néel energy.

In the previous two sets of studies, it was observed the angular momentum tends to be better conserved in the z direction. To investigate why, we examined the effect of initial magnetization direction on the total angular momentum and magnetization for three different initial magnetizations: [100] (x direction), [001] (z direction), and [111] (mixed direction). EAM, shifted force exchange, and shifted force Néel with the fitted α_l and α_q values were used for this study. Figs. 6 and 7 show the results for an isolated cube and for a bulk periodic system, respectively. For both geometries it is evident that that angular momentum is best conserved in the direction of initial magnetization. For example, Figs. 6(d) and 7(d) indicate that samples with an initial [100] magnetization remain strongly magnetized in the x direction even after thermalization, and Figs. 6(a) and 7(a) show negligible drift of the x-component of angular momentum. In contrast, the y and z directions are almost demagnetized, with evident drifts in the y- and z-direction magnetization. Figs. 6(e), 7(e), 6(b), and 7(b) tell a similar story for samples with initial [001] magnetization: angular momentum is well conserved in the z direction. For samples with [111] initialization, Figs. 6(f), 7(f), 6(c), and 7(c) show that there is no preferred magnetization direction after initialization and that angular momentum drifts are present in all coordinate directions.

A trend similar to the one observed in Figs. 6(b) and 6(e) was reported in Ref. [7]. In that study, a 50 T field applied to an isolated nanoparticle in the z direc-

tion yielded angular momentum conservation in the z direction, but not in x or y directions due to symmetry breaking. Interestingly, no external field was necessary to achieve this result in our case. It appears that the internal effective field $\boldsymbol{\omega}_i$ acting on each atom as a result of exchange and Néel interactions is strong enough to magnetize the sample in the z direction and achieve a similar effect.
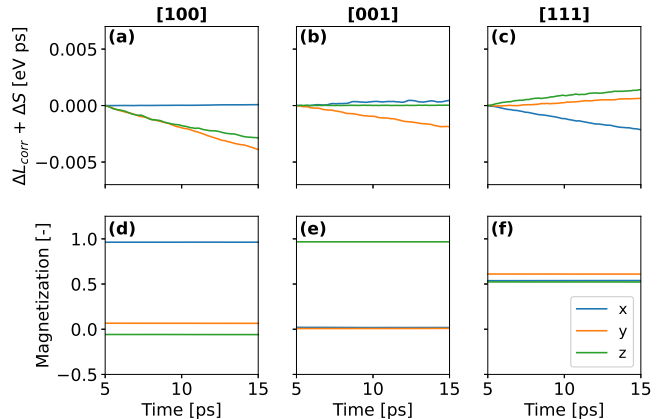

FIG. 6: Dependence of total open system angular momentum and magnetization on initial magnetization direction for an isolated cube. Magnetizations initialized in (a,d) [100] direction, (b,e) [001] direction, (c,f) [111] direction.
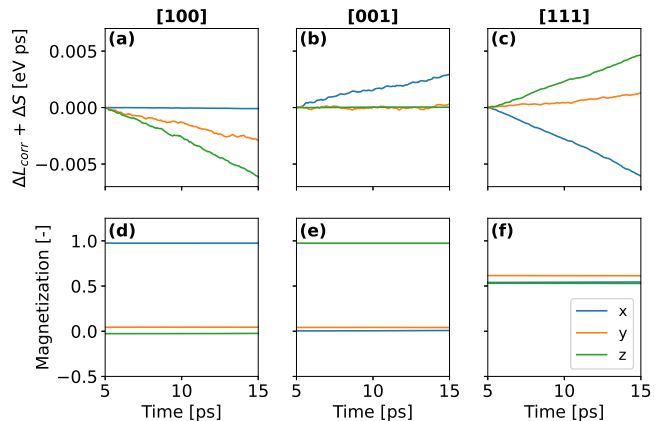

FIG. 7: Dependence of total open system angular momentum and magnetization on initial magnetization direction for a bulk periodic system. Magnetizations initialized in (a,d) [100] direction, (b,e) [001] direction, (c,f) [111] direction.

C. Theoretical Justification of Total Angular Momentum Conservation with Néel Anisotropy

Dednam et al. [13] showed theoretically that exchange and uniaxial Hamiltonians conserve total angular mo-

mentum $\mathcal{J}$. Here we follow the approach in [13] to do the same for Néel anisotropy. We analyze the pseudo-dipole term below. The pseudo-quadrupole term is more complicated and produces qualitatively similar results (one force component perpendicular to the bond and one parallel to the bond), so it is omitted for clarity.

The rate of change of the spin angular momentum of particle i is $d\mathbf{S}_i/dt$. Substituting Eqs.(5), (8), and (10) yields

$$\frac{d\mathbf{S}_i}{dt} = \frac{\partial \mathcal{H}}{\partial \mathbf{s}_i} \times \mathbf{s}_i. \tag{43}$$

Substituting the Hamiltonian for the pseudo-dipole Néel term from Eq. (18)

$$\mathcal{H}_{Neel,d} = -\frac{1}{2} \sum_{i,j=1,i\neq j}^{N} l_1(r_{ij}) \Big((\mathbf{e}_{ij} \cdot \mathbf{s}_i)(\mathbf{e}_{ij} \cdot \mathbf{s}_j) \\ -\frac{\mathbf{s}_i \cdot \mathbf{s}_j}{3} - \frac{2}{3} \Big) \tag{44}$$

and taking the derivative with respect to $\mathbf{s}_i$ yields

$$\frac{\partial \mathcal{H}_{Neel,d}}{\partial \mathbf{s}_i} = -\Big[\sum_{j=1,i\neq j}^{N} l_1(r_{ij}) \Big((\mathbf{e}_{ij} \cdot \mathbf{s}_j)\mathbf{e}_{ij} - \frac{\mathbf{s}_j}{3} \Big) \Big] \tag{45}$$

and

$$\frac{d\mathbf{S}_i}{dt} = -\Big[\sum_{j=1,i\neq j}^{N} l_1(r_{ij}) \Big((\mathbf{e}_{ij} \cdot \mathbf{s}_j)\mathbf{e}_{ij} - \frac{\mathbf{s}_j}{3} \Big) \Big] \times \mathbf{s}_i. \tag{46}$$

The above expression shows that the rate of change of atom i's spin angular momentum has contributions from all atoms that interact with i. The contribution of a single atom j to atom i's spin angular momentum rate, denoted here as $d\mathbf{S}_{ij}/dt$, is written as

$$\frac{d\mathbf{S}_{ij}}{dt} = -l_1(r_{ij}) \Big((\mathbf{e}_{ij} \cdot \mathbf{s}_j)\mathbf{e}_{ij} - \frac{\mathbf{s}_j}{3} \Big) \times \mathbf{s}_i. \tag{47}$$

Similarly, the contribution of a single atom i to atom j's spin angular momentum rate can be written as

$$\frac{d\mathbf{S}_{ji}}{dt} = -l_1(r_{ji}) \Big((\mathbf{e}_{ji} \cdot \mathbf{s}_i)\mathbf{e}_{ji} - \frac{\mathbf{s}_i}{3} \Big) \times \mathbf{s}_j. \tag{48}$$

Recognizing that $r_{ij} = r_{ji}$ and that $(\mathbf{e}_{ji} \cdot \mathbf{s}_i)\mathbf{e}_{ji} = (\mathbf{e}_{ij} \cdot \mathbf{s}_i)\mathbf{e}_{ij}$ due to cancellation of negative signs yields

$$\frac{d\mathbf{S}_{ji}}{dt} = -l_1(r_{ij}) \Big((\mathbf{e}_{ij} \cdot \mathbf{s}_i)\mathbf{e}_{ij} - \frac{\mathbf{s}_i}{3} \Big) \times \mathbf{s}_j. \tag{49}$$

The sum of these two expressions represents the rate of change of spin angular momentum of the i-j pair caused by Néel anisotropy interactions between atoms i and j:

$$\frac{d\mathbf{S}_{ij}}{dt} + \frac{d\mathbf{S}_{ji}}{dt} = -l_1(r_{ij}) \Big((\mathbf{e}_{ij} \cdot \mathbf{s}_j)\mathbf{e}_{ij} \times \mathbf{s}_i \\ +(\mathbf{e}_{ij} \cdot \mathbf{s}_i)\mathbf{e}_{ij} \times \mathbf{s}_j \Big). \tag{50}$$

The contribution of Néel anisotropy to the lattice angular momentum is discussed next. The rate of change of lattice angular momentum of the i-j pair caused by pairwise forces acting between atoms i and j is written as [13]

$$\frac{d\mathbf{L}_{ij}}{dt} + \frac{d\mathbf{L}_{ji}}{dt} = (\mathbf{r}_i - \mathbf{r}_j) \times \mathbf{f}_{ij} \tag{51}$$

where $\mathbf{f}_{ij}$ is defined as the force exerted on atom i by atom j. Substituting the Néel pseudo-dipole Hamiltonian into Eq. (9) yields

$$\mathbf{f}_{i,Neel,d} = \sum_{j=1,j\neq i}^{N} \Big[\Big(\frac{\partial l_1(r_{ij})}{\partial r_{ij}} - \frac{2l_1(r_{ij})}{r_{ij}} \Big) \\ (\mathbf{e}_{ij} \cdot \mathbf{s}_i)(\mathbf{e}_{ij} \cdot \mathbf{s}_j) - \frac{\partial l_1(r_{ij})}{\partial r_{ij}} \Big(\frac{\mathbf{s}_i \cdot \mathbf{s}_j}{3} + \frac{2}{3} \Big) \Big] \mathbf{e}_{ij} \\ + \frac{l_1(r_{ij})}{r_{ij}} (\mathbf{e}_{ij} \cdot \mathbf{s}_j)\mathbf{s}_i + \frac{l_1(r_{ij})}{r_{ij}} (\mathbf{e}_{ij} \cdot \mathbf{s}_i)\mathbf{s}_j. \tag{52}$$

Considering only a single term from the summation yields

$$\mathbf{f}_{ij} = \Big[\Big(\frac{\partial l_1(r_{ij})}{\partial r_{ij}} - \frac{2l_1(r_{ij})}{r_{ij}} \Big) (\mathbf{e}_{ij} \cdot \mathbf{s}_i)(\mathbf{e}_{ij} \cdot \mathbf{s}_j) \\ - \frac{\partial l_1(r_{ij})}{\partial r_{ij}} \Big(\frac{\mathbf{s}_i \cdot \mathbf{s}_j}{3} + \frac{2}{3} \Big) \Big] \mathbf{e}_{ij} \\ + \frac{l_1(r_{ij})}{r_{ij}} (\mathbf{e}_{ij} \cdot \mathbf{s}_j)\mathbf{s}_i + \frac{l_1(r_{ij})}{r_{ij}} (\mathbf{e}_{ij} \cdot \mathbf{s}_i)\mathbf{s}_j. \tag{53}$$

Recognizing that the cross product $(\mathbf{r}_i - \mathbf{r}_j) \times \mathbf{e}_{ij}$ is zero because the vectors are parallel reduces the above equation to:

$$\frac{d\mathbf{L}_{ij}}{dt} + \frac{d\mathbf{L}_{ji}}{dt} = (\mathbf{r}_i - \mathbf{r}_j) \times \Big(\frac{l_1(r_{ij})}{r_{ij}} (\mathbf{e}_{ij} \cdot \mathbf{s}_j)\mathbf{s}_i \\ + \frac{l_1(r_{ij})}{r_{ij}} (\mathbf{e}_{ij} \cdot \mathbf{s}_i)\mathbf{s}_j \Big). \tag{54}$$

Factoring out $l_1(r_{ij})$ and substituting $\mathbf{e}_{ij} = (\mathbf{r}_i - \mathbf{r}_j)/r_{ij}$ leads to

$$\frac{d\mathbf{L}_{ij}}{dt} + \frac{d\mathbf{L}_{ji}}{dt} = l_1(r_{ij}) \Big((\mathbf{e}_{ij} \cdot \mathbf{s}_j)\mathbf{e}_{ij} \times \mathbf{s}_i \\ +(\mathbf{e}_{ij} \cdot \mathbf{s}_i)\mathbf{e}_{ij} \times \mathbf{s}_j \Big). \tag{55}$$

Combining the pairwise rates of change of spin and lattice angular momentum from Eqs. (50) and (55) gives

$$\frac{d\mathbf{S}_{ij}}{dt} + \frac{d\mathbf{S}_{ji}}{dt} + \frac{d\mathbf{L}_{ij}}{dt} + \frac{d\mathbf{L}_{ji}}{dt} = \frac{d\mathcal{J}_{ij}}{dt} + \frac{d\mathcal{J}_{ji}}{dt} = 0. \tag{56}$$

The pairwise total angular momentum is thus conserved for Néel anisotropy.

VI. ENERGY CONSERVATION IN SPIN-LATTICE DYNAMICS

A. EAM and Exchange

In Section V, we investigated angular momentum conservation in SLD, and found that angular momentum exchange between spin and lattice systems only occurs when an anisotropic energy term is included in the Hamiltonian. We also found that total angular momentum is approximately conserved in the magnetization direction, even in the absence of an external applied field, and that reducing the magnitude of the anisotropic energy improves the angular momentum conservation. Here we investigate energy conservation, which can be an issue when using the explicit Suzuki-Trotter decomposition method to solve the equations of motion for SLD [1, 5]. To understand how energy is exchanged between spin and lattice systems governed by purely isotropic interactions, we first investigate systems with only EAM and shifted force exchange terms in the Hamiltonian. Using the same simulation procedure and cube geometry described in Section V, we computed energy per atom $\Delta E = [E(t) - E(5\ ps)]/N$ separately for lattice and magnetic systems. As with angular momentum, these energies were measured relative to their values at 5 ps, which was when the spin and lattice thermostats were turned off. They are plotted in Fig. 9 for a simulation whose Langevin thermostats were initialized with a seed value of 21.

Unlike Fig. 3 for EAM and shifted force exchange, which shows that the lattice and spin systems do not exchange angular momentum, Fig. 8 shows that energy is exchanged between the two systems. The mirror image plots of lattice energy (blue) and spin energy (orange), along with the flat line for total energy, illustrate that energy is well conserved. A linear fit to the total energy, performed between 5 and 45 ps using the package sci-kit learn [21], yields a slight energy drift of -2.38×10^{-11} eV/ps/atom. The total energy change over the 45 ps of the simulation is estimated from this drift as -1.07×10^{-9} eV/atom, which is 6 orders of magnitude smaller than the lattice and spin energy fluctuations in Fig. 8. An important takeaway from the comparison between Figs. 3 and 8 is that energy coupling between spin and lattice systems is not sufficient to guarantee angular momentum coupling or angular momentum conservation.
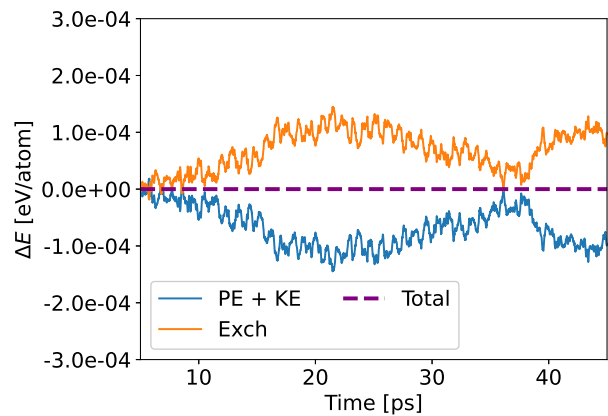

FIG. 8: Relative values of lattice energy, spin energy, and total energy for an isolated cube using the EAM and shifted force exchange Hamiltonians.

B. EAM, Exchange, and Néel

Next, the Néel anisotropy energy was added to the Hamiltonian. The results (Fig 9a) are similar to those that did not include the Néel term: spin and lattice energies are well coupled and total system energy is conserved. A noteworthy point here is that the energy drift $(-1.58 \times 10^{-7}$ eV/ps/atom) is much larger than that without the Néel anisotropy term, although the total energy change over 45 ps is still negligible compared to the lattice and spin energy fluctuations. This energy drift is also larger than that observed in Ref. [7], which analyzed cobalt nanocubes in a 50 T field using the Suzuki Trotter decomposition method.

We hypothesize that this may arise from the different functional forms of the Néel anisotropy energy used in the two studies. This is explained as follows. The magnetic anisotropy energy depends on atomic positions, and thus exerts forces on the atoms. These forces are usually calculated using Eq. (1) [1, 3, 6, 7, 13], but this process is not fully justified for for Eq. (18) because it does not produce purely central forces. The Néel energy depends on both the magnitude and direction of the position vector between atomic pairs, and the application of Eq. (1) to it generates forces whose directions are determined by a weighted vector sum of $\mathbf{r}_{ij}$, $\mathbf{s}_i$, and $\mathbf{s}_j$. This is shown in Eq. (52). The noncentral forces arising from the components of $\mathbf{s}_i$ and $\mathbf{s}_j$ that are perpendicular to $\mathbf{r}_{ij}$ are nonconservative and they torque the atomic bonds to drive angular momentum transfer between spins and lattice in the simulations.

Our Néel anisotropy energy differs from the anisotropy used in Ref. [7] in two ways: the $\mathbf{s}_i \cdot \mathbf{s}_j/3 + 2/3$ term, which is missing in Ref. [7], and the energy scale l_1, which here is given by the sum of shifted force Bethe-Slater functions in Eq. (19) and which in Ref. [7] varies as r_{ij}^{-4}. Either difference could potentially lead to differences in energy drift. In particular, the $\mathbf{s}_i \cdot \mathbf{s}_j/3 + 2/3$

term is generally positive for most atom pairs because the samples are strongly magnetized. Subtraction of this positive term in Eq. (52) leads to a weaker conservative ($\mathbf{e}_{ij}$-directed) force component such that the nonconservative force is a larger fraction of the total atomic force in our simulations relative to Ref. [7]. Nonconservative forces may pose challenges for Suzuki-Trotter integration, which is rigorously only applicable to conservative systems [22]. It is possible that the larger energy drifts in our simulations are related to the increased contribution of nonconservative forces.

This is supported by studies in which we varied the strength of the Néel energy term to 10% and 1% of the Neel dipole and quadrupole energy scales in Table I. While energy was still well conserved on the scale of lattice and magnetic energy fluctuations (Figs. 9(b-c)), we discovered that energy drifts scale linearly with the strength of the Neel term. The 10% and 1% cases yielded 1 and 2 order of magnitude reductions in energy drifts (-1.85×10^{-8} and -1.70×10^{-9} eV/ps/atom, respectively.)
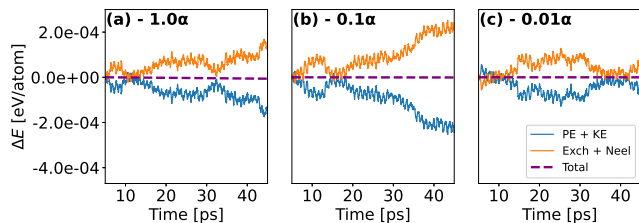

FIG. 9: Relative values of lattice energy, spin energy, and total energy for an isolated cube using the EAM, shifted force exchange, and shifted force Néel Hamiltonians for different Néel energy parameterizations α_l and α_q . (a) Néel energy values from Table I, (b) 10% of Néel values in Table I, (c) 1% of Néel values in Table I.

C. Timestep Effects

The Suzuki-Trotter method [19] suffers from energy drifts that arise from errors in the numerical integration scheme [5]. These errors scale as Δt^3 [4, 19].To understand the present energy drifts better, we examined their time step dependence for four cases of Hamiltonian. Figure 11 shows the results for EAM and shifted force exchange Hamiltonians with shifted force Néel anisotropy energy strengths of 0%, 1%, 10%, and 100%. The results for each case are averaged over three different initializations.

The timestep dependence of energy drift in the case of EAM and exchange follows the expected Δt^3 behavior. However, addition of the Néel anisotropy energy, even at levels as small as 1% of the nominal strength, results in a linear rather than cubic dependence of drift on time step. This drift, as discussed in the previous section, also scales linearly with the strength of the Néel interaction. We

believe that the linear dependence on timestep for cases that include Néel anisotropy energy is a consequence of the nonconservative forces it introduces. Similar linear drifts have been found in numerical simulations of the evolution of galaxies [22].
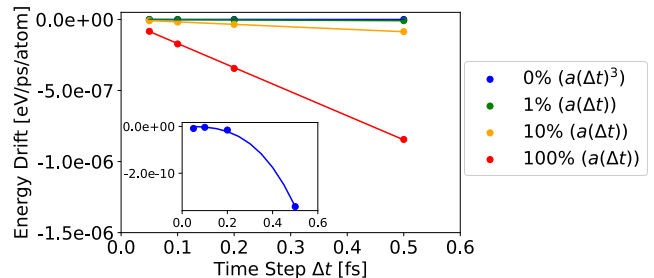

FIG. 10: Total energy drifts for SLD simulations of an isolated cube using the EAM, shifted force exchange, and shifted force Néel Hamiltonians with different Néel energy scales.

VII. CONCLUSIONS

The Suzuki-Trotter explicit integrator used in the SPIN package in LAMMPS has been updated to account for transport and generation of lattice angular momentum in periodic systems. Inclusion of these mechanisms yields exact conservation of angular momentum in molecular dynamics simulations with periodic boundary conditions. However, simulations of bulk systems and cubic nanoparticles show that total angular momentum is not conserved in spin-lattice dynamics systems that only have isotropic exchange interactions, because the central magnetic forces generated in such systems are unable to torque the bonds of the lattice. The addition of a Néel anisotropy energy term generates noncentral, nonconservative forces that couple the spins and the lattice, but that also generate energy drifts significantly higher than those found in simulations with only exchange interactions. These drifts, which scale linearly with the magnitude of Néel anisotropy energy, may be a consequence of applying the Suzuki-Trotter integrator to a system with nonconservative forces.

ACKNOWLEDGMENTS

Appendix: Implementation in SLD Solver

The conservation of angular momentum theory outlined in Section III A for open systems was implemented in the SPIN package [1] of the 3Mar20 release of LAMMPS [15], which uses the Suzuki-Trotter decomposition method to integrate the equations of motion. The pseudo code that outlines the implementation of this method is outlined in Figure 11.

The modified angular momentum method is implemented in the Suzuki-Trotter decomposition integrator as follows. Initially, the torque $\mathbf{T}$ on each atom i in the simulation box is computed using forces from the image atoms, and the lattice angular momentum is also computed. The variable $\mathbf{rp}$ in this calculation is a wrapped atom coordinate vector advanced at each time step along with the corresponding unwrapped coordinate vector $\mathbf{r}$. Differences between $\mathbf{r}$ and $\mathbf{rp}$ are used to identify which atom crosses the boundary and the exact time step at which the crossing occurs. This information is used to update the vector $\mathbf{rid}$, which is used to store image flags. If an atom wraps around the simulation box as it moves in a positive (negative) coordinate direction, its image flag is set to 1 (-1). Otherwise it is set to zero. The value of $\mathbf{rid}$ is used to calculate the particle transport term $\mathbf{Q}$. Then, following the procedure in the SPIN package, the Suzuki-Trotter decomposition advances the velocities a half time step, the spins two quarter time steps, the unwrapped and wrapped positions a full time step, and the spins the final two quarter time steps. In this decomposition, the angular frequency vector is updated every quarter time step to compute spins at the subsequent quarter time step. The total ($\mathbf{f}$) and image ($\mathbf{f}_{image}$) forces imparted on the atoms are calculated using the updated positions at time $t + \Delta t$. Newton's third law has been turned off via the LAMMPS setting "newton off off" to facilitate the separate computation of $\mathbf{f}$ and $\mathbf{f}_{image}$. The net lattice angular momentum influx during Δt is then calculated using the velocity at time $t + \Delta t/2$ because that is the velocity with which the atoms cross the boundary. The velocity at $t + \Delta t$ is then computed, completing the Suzuki-Trotter decomposition method. Finally, the torque and angular momentum are computed at $t + \Delta t$, the torque is integrated from t to $t + \Delta t$, the modified angular momentum is found using the trapezoidal rule, and the modified angular momentum $\mathbf{L}_{corr}$ is calculated.

```
% Initialization (t = 0)
for all atoms do
    T[t] = compute_torque(f_image[t], rp[t])    ▷ Eq. (38)
    L[t] = compute_angular_momentum(rp[t], v[t], m)
        ▷ Eq. (3)

% Initial Integration
for all atoms do
    v[t + Δt/2] = compute_velocity(v[t], f[t], m)
    s[t + Δt/4] = compute_spin(s[t],
        compute_omega(s[t], r[t]));
    s[t + 2Δt/4] = compute_spin(s[t + Δt/4],
        compute_omega(s[t + Δt/4], r[t]));
    r[t + Δt] = compute_position(r[t], v[t + Δt/2]);
    rp[t + Δt] = compute_position(rp[t], v[t + Δt/2]);
    s[t + 3Δt/4] = compute_spin(s[t + 2Δt/4],
        compute_omega(s[t + 3Δt/4], r[t + Δt]));
    s[t + Δt] = compute_spin(s[t + 3Δt/4],
        compute_omega(s[t + 3Δt/4], r[t + Δt]));

% Periodic Wrapping
for all atoms do
    if rp[t + Δt] > 0.0 & rp[t + Δt] < Box then
        rid[t + Δt] = 0;
    if rp[t + Δt] < 0.0 then
        rp[t + Δt] = rp[t + Δt] + Box;
        rid[t + Δt] = −1;
    if rp[t + Δt] > Box then
        rp[t + Δt] = rp[t + Δt] − Box;
        rid[t + Δt] = 1;

% Force Calculation
for all atoms do
    f[t + Δt], f_image[t + Δt] = compute_force(rp[t + Δt])

% Wrapping Momentum Flux
for all atoms do
    Qdt[t + Δt] = compute_flux(rp[t + Δt], rid[t +
        Δt], v[t + Δt/2], m);              ▷ Eq. (41)

% Final Integrate
for all atoms do
    v[t + Δt] = compute_velocity(v[t + Δt/2],
        f[t + Δt], m);

% Image Atom Torque & Angular Momentum
  Calculation
for all atoms do
    T[t + Δt] =
        compute_torque(f_image[t + Δt], rp[t + Δt]);  ▷ Eq.
        (38)
    Tdt[t + Δt] = compute_torque_integral(T[t],
        T[t + Δt]);                        ▷ Eq. (40)
    L[t + Δt] = compute_angular_momentum(rp[t +
        Δt], v[t + Δt], m);                ▷ Eq. (3)
    L_corr[t + Δt] =
        compute_modified_angular_momentum(L[t + Δt],
        Qdt[t + Δt], Tdt[t + Δt]);         ▷ Eq. (42)
```

FIG. 11: Overview of the Suzuki-Trotter decomposition method with conservation of momentum tracking.

[1] J. Tranchida, S. Plimpton, P. Thibaudeau, and A. P. Thompson, Journal of Computational Physics **372**, 406 (2018).

[2] P.-W. Ma, C. Woo, and S. Dudarev, Physical review B **78**, 024434 (2008).

[3] D. Perera, M. Eisenbach, D. M. Nicholson, G. M. Stocks, and D. P. Landau, Physical Review B **93**, 060402 (2016).

[4] J. R. Cooke III and J. R. Lukes, Computer Physics Communications **271**, 108203 (2022).

[5] D. Beaujouan, P. Thibaudeau, and C. Barreteau, Physical Review B **86**, 174409 (2012).

[6] M. Strungaru, M. O. Ellis, S. Ruta, O. Chubykalo-Fesenko, R. F. Evans, and R. W. Chantrell, Physical Review B **103**, 024429 (2021).

[7] M. Aßmann and U. Nowak, Journal of Magnetism and Magnetic Materials **469**, 217 (2019).

[8] X. Wu, Z. Liu, and T. Luo, Journal of Applied Physics **123**, 085109 (2018).

[9] M. P. Allen and D. J. Tildesley, *Computer simulation of liquids* (Oxford university press, 2017).

[10] D. Frenkel and B. Smit, *Understanding molecular simulation: from algorithms to applications*, Vol. 1 (Elsevier, 2001).

[11] R. F. Evans, W. J. Fan, P. Chureemart, T. A. Ostler, M. O. Ellis, and R. W. Chantrell, Journal of Physics: Condensed Matter **26**, 103202 (2014).

[12] O. Eriksson, A. Bergman, L. Bergqvist, and J. Hellsvik, *Atomistic spin dynamics: foundations and applications* (Oxford university press, 2017).

[13] W. Dednam, C. Sabater, A. E. Botha, E. B. Lombardi, J. Fernández-Rossier, and M. J. Caturla, Computational Materials Science **209**, 111359 (2022).

[14] V. A. Kuzkin, ZAMM-Journal of Applied Mathematics and Mechanics/Zeitschrift für Angewandte Mathematik und Mechanik **95**, 1290 (2015).

[15] S. Plimpton, Journal of computational physics **117**, 1 (1995).

[16] H. Chamati, N. Papanicolaou, Y. Mishin, and D. Papaconstantopoulos, Surface Science **600**, 1793 (2006).

[17] S. Toxvaerd and J. C. Dyre, The Journal of Chemical Physics **134**, 081102 (2011).

[18] P. Nieves, J. Tranchida, S. Arapan, and D. Legut, Physical Review B **103**, 094437 (2021).

[19] I. Omelyan, I. Mryglod, and R. Folk, Physical review letters **86**, 898 (2001).

[20] I. Omelyan, I. Mryglod, and R. Folk, Physical Review E **64**, 016105 (2001).

[21] F. Pedregosa, G. Varoquaux, A. Gramfort, V. Michel, B. Thirion, O. Grisel, M. Blondel, P. Prettenhofer, R. Weiss, V. Dubourg, J. Vanderplas, A. Passos, D. Cournapeau, M. Brucher, M. Perrot, and E. Duchesnay, Journal of Machine Learning Research **12**, 2825 (2011).

[22] H. Rein and D. S. Spiegel, Monthly Notices of the Royal Astronomical Society **446**, 1424 (2015).

[23] J. Towns, T. Cockerill, M. Dahan, I. Foster, K. Gaither, A. Grimshaw, V. Hazlewood, S. Lathrop, D. Lifka, G. D. Peterson, *et al.*, Computing in science & engineering **16**, 62 (2014).

[24] N. A. Nystrom, M. J. Levine, R. Z. Roskies, and J. R. Scott, in *Proceedings of the 2015 XSEDE Conference: Scientific Advancements Enabled by Enhanced Cyberinfrastructure* (2015) pp. 1–8.